









Gamma-ray detection of newly discovered Ancora supernova remnant: G288.8–6.3

Christopher Burger-Scheidlin^{1,2}, Robert Brose^{1,3}, Jonathan Mackey^{1,2}, Miroslav D. Filipović⁴,
Pranjupriya Goswami^{5,6}, Enrique Mestre Guillen⁷, Emma de Oña Wilhelmi⁸, and Iurii Sushch^{6,9,10}

¹ Dublin Institute for Advanced Studies, Astronomy & Astrophysics Section, DIAS Dunsink Observatory, Dublin D15 XR2R, Ireland
e-mail: cburger@cp.dias.ie

² School of Physics, University College Dublin, Belfield, Dublin D04 V1W8, Ireland

³ School of Physical Sciences and Centre for Astrophysics & Relativity, Dublin City University, D09 W6Y4 Glasnevin, Ireland

⁴ Western Sydney University, Locked Bag 1797, Penrith South DC, NSW 2751, Australia

⁵ Université Paris Cité, CNRS, Astroparticule et Cosmologie, 75013 Paris, France

⁶ Centre for Space Research, North-West University, 2520 Potchefstroom, South Africa

⁷ Institute of Space Sciences (ICE, CSIC), Campus UAB, Carrer de Can Magrans s/n, 08193 Barcelona, Spain

⁸ Deutsches Elektronen-Synchrotron DESY, Platanenallee 6, 15738 Zeuthen, Germany

⁹ Astronomical Observatory of Ivan Franko National University of Lviv, Kyryla i Methodia 8, 79005 Lviv, Ukraine

¹⁰ Gran Sasso Science Institute, Via F. Crispi 7, 67100 L'Aquila, Italy

Received 22 October 2023 / Accepted 23 January 2024

ABSTRACT

Context. The supernova remnant (SNR) G288.8–6.3 was recently discovered as a faint radio shell at high Galactic latitude using observations with the Australian Square Kilometre Array Pathfinder (ASKAP) in the Evolutionary Map of the Universe (EMU) survey.

Aims. We performed the first detailed investigation of the γ -ray emission from the G288.8–6.3 region, aiming to characterise the high-energy emission in the GeV regime from the newly discovered SNR, dubbed Ancora.

Methods. Fifteen years of *Fermi*-Large Area Telescope (LAT) data were analysed at energies between 400 MeV and 1 TeV, and the excess seen in the region was modelled using different spatial and spectral models.

Results. We detect spatially extended γ -ray emission coinciding with the radio SNR, with detection significance up to 8.8σ . A radial disk spatial model in combination with a power-law spectral model with an energy flux of $(4.80 \pm 0.91) \times 10^{-6} \text{ MeV cm}^{-2} \text{ s}^{-1}$, with the spectrum extending up to around 5 GeV was found to be the preferred model. Morphologically, hotspots seen above 1 GeV are well correlated with the bright western part of the radio shell. The emission is more likely to be of leptonic origin, given the estimated gas density in the region and the estimated distance and age of the SNR, but a hadronic scenario cannot be ruled out.

Conclusions. Ancora is the seventh confirmed SNR detected at high Galactic latitude with *Fermi*-LAT. The study of this new population of remnants can provide insights into the evolutionary aspects of SNRs and their properties, and further advance efforts of constraining the physics of particle diffusion and escape from SNRs into the Galaxy.

Key words. cosmic rays – ISM: supernova remnants – gamma rays: ISM – radio continuum: ISM – ISM: individual objects: G288.8–6.3 (Ancora SNR)

1. Introduction

After the detection of cosmic rays (CRs) through observations of ionising radiation made on multiple balloon flights by Victor Hess (Hess 1912), their spectrum was subsequently measured by many experiments (e.g. Tanabashi et al. 2018; Filipović & Tothill 2021). The current consensus is that cosmic protons with energies up to 3×10^{15} eV have Galactic origin (Aloisio et al. 2012; Globus et al. 2015). Supernova remnants (SNRs) have been traditionally considered to be prime candidates for the acceleration of these particles to high energies, and were first suggested as sources by Baade & Zwicky (1934). The number of currently detected and confirmed SNRs is close to three hundred (Green 2017, 2019), the majority of them first detected at radio wavelengths. Around 10% were subsequently also detected at γ -ray energies (Acero et al. 2016). There are only about ten remnants where non-thermal X-ray synchrotron emission was seen (Vink 2012), and even fewer were detected at very high-energy (VHE) γ -rays (e.g. H.E.S.S. Collaboration 2018).

Recently, the population of high-latitude supernova remnants has received some attention. Ackermann et al. (2018) reported the detection of SNR candidates amongst the analysed sources, and other confirmed detections include G296.5+10.0 and G166.0+4.3 (Araya 2013), G150+4.5 (Devin et al. 2020), G17.8+16.7 (Araya et al. 2022), and Calvera SNR (Arias et al. 2022 and Araya 2023) emitting in this high-energy γ -ray regime.

In their first published SNR catalogue the *Fermi* collaboration classify 30 sources as likely GeV SNRs, as well as four marginal associations and 245 flux upper limits (Acero et al. 2016). Although instruments have improved significantly since early high-energy surveys for SNRs (e.g. EGRET; Sturmer & Dermer 1995; Esposito et al. 1996), the limited spatial resolution and photon statistics in γ -rays make new discoveries challenging. Most SNRs are therefore first identified by their distinctive non-thermal radio spectrum and shell-like morphology. Observations at high energies allow for a much more detailed understanding of the physical phenomena taking place at the sources. They potentially permit us to distinguish between

leptonic and hadronic emission scenarios (e.g. Aharonian et al. 2007), and allow us to constrain maximum particle energies (e.g. Abeyssekara et al. 2020). Morphological differences between wavelength bands can also give insight into where particle acceleration is taking place and how CRs escape from SNRs into the Galaxy. Furthermore, increasing the number of SNRs detected at high energies enables comparisons between these different sources, enhances our understanding of the population class to find common spectral and spatial features, and identifies unexpected properties.

Here we report the detection of extended γ -ray emission spatially coincident with the shell of a newly discovered radio SNR. Ancora SNR¹ (also known as G288.8–6.3) at a high Galactic latitude of -6.3° was first detected by Filipović et al. (2023) through multi-frequency analysis of Australian Square Kilometre Array Pathfinder (ASKAP) data. The authors reported a low-radio-surface-brightness SNR with a shell-like structure extending to a diameter of $1.8^\circ \times 1.6^\circ$. They estimate the distance at ≈ 1.3 kpc, implying an offset of 140 pc above the Galactic plane, and the age of the remnant, based on the surface brightness, at >13 kyr.

The detection in radio continuum wavebands, with strong hints of non-thermal emission, has sparked the efforts to analyse the region at γ -ray energies using the *Fermi*-LAT instrument. In the following sections, we show how we performed the analysis of LAT data, which models were considered to fit the excess emission (Sect. 2), which major results we were able to obtain from the best-fit models, and how they relate to other instruments (Sect. 3). In Sect. 4, we discuss our findings in the context of the other high-latitude SNRs and the potential for further detections at higher and lower energies. Finally, we present our conclusions in Sect. 5.

2. *Fermi*-LAT data analysis

2.1. Data reduction

We used 15 yr of *Fermi*-LAT Pass 8 data (August 2008–July 2023, correspondingly 239 557 417–712 342 367 *Fermi* mission elapsed time, MET) using the P8R3_SOURCE class events (Atwood et al. 2013). The selected data were within a radius of 12° in the region of interest (ROI) around the centre of the detected radio SNR at Galactic position GLON/GLAT = $288.8^\circ/-6.3^\circ$ (corresponding to RA/Dec = $157.488^\circ/-65.214^\circ$) in an energy range between 400 MeV and 1 TeV. We only analysed data above 400 MeV to decrease the uncertainties due to the poorer angular resolution, given the large size of the SNR. Additionally, cuts on the PSF class were made by employing `evtype = 56`, discarding the lowest-quality quartile data in terms of event direction reconstruction (i.e. PSF0 class events).

The data were analysed using the Python package *Fermipy* (v1.1.6, Wood et al. 2017) and the *Fermitools* software package (v2.2.0²) following the standard procedure of the binned maximum-likelihood analysis technique together with the P8R3_V3 instrument response functions. The recommended filters (`DATA_QUAL > 0` && `LAT_CONFIG == 1`) were used for data reduction, and zenith angle cuts of 90° were applied to reduce contamination from the direction of Earth’s atmosphere. Regarding spatial binning, a pixel size of 0.1° was applied

with eight logarithmic energy bins per decade. The underlying source catalogue used was the fourth *Fermi* catalogue (Abdollahi et al. 2020), specifically the incremental Data Release 3 version 4FGL-DR3 (Abdollahi et al. 2022), modelling sources that were lying up to 3° outside the ROI. To account for diffuse emission, we applied the Galactic diffuse emission model (`gll_iem_v07.fits`) with an isotropic component corresponding to the chosen event class (`iso_P8R3_SOURCE_V3_v1.txt`).

2.2. Morphological and spectral analysis

Excess emission from SNR G288.8–6.3 has only recently been discovered at radio wavelengths (954 MHz) with ASKAP by Filipović et al. (2023). The authors found a spatial extension of $1.8^\circ \times 1.6^\circ$ in diameter of this faint low-surface-brightness radio source. When searching for excess in γ -rays, we analysed the energy range between 400 MeV to 1 TeV, and later made cuts on the energy range to confirm the extension, and to find morphological features and excess at higher energies where the point spread function (PSF) of the *Fermi*-LAT instrument is much better compared to lower energies³. Except for one source, namely 4FGL J1028.7–6431c (henceforth J1028), all sources in the 4FGL-DR3 catalogue around the target position were at distances greater than 1.3° from the centre of the radio source. J1028 is located around 0.7° from the centre of the SNR, and is thus roughly overlapping with the northern part of its shell. It is catalogued as a slightly elongated source with a 68 % containment radius of $\sim 0.12^\circ$, and a log-parabola spectral model of the form

$$\frac{dN}{dE} = N_0 \left(\frac{E}{E_0} \right)^{-\alpha - \beta \log(E/E_0)}, \quad (1)$$

with an energy flux $N_0 = (1.5 \pm 0.3) \times 10^{-12} \text{ MeV}^{-1} \text{ cm}^{-2} \text{ s}^{-1}$, $\alpha = 2.6 \pm 0.3$, and $\beta = 0.4 \pm 0.2$, and a pivot energy of $E_0 = 720 \text{ MeV}$. It has a detection significance of 5.6σ . An association with PMN J1028–6441 was claimed earlier (Abdollahi et al. 2022).

To test different models, J1028 was removed from some of the analyses for comparison of the goodness of fit. Spectral parameters of the sources within the 3° were left free during fitting, as were the normalisation factors of sources above a test statistic⁴, $TS = 10$ within the ROI. The parameters of all other sources were kept fixed to their 4FGL-DR3 catalogue values. We applied the energy dispersion correction for all sources apart from the isotropic diffuse emission background model. We performed three initial optimisations of the sources using the `optimize()` method, which attempts a preliminary fit to ensure that parameters are close to their maximum likelihood values, and then an initial fit using the `fit()` method with the *newminuit* optimiser. Afterwards, we removed sources with $TS < 1$. Further fitting showed that no additional sources with $TS < 1$ appeared. Subsequently, we added different extended spatial models (*RadialDisk* and *RadialGaussian*) using the `add_source()` method at the known radio source position (GLON/GLAT = $288.8^\circ/-6.3^\circ$) with their default extension parameters, and refitted the region. Then, the `extension()` method provided in *Fermipy* was applied to determine the best-fit radius iterating between the extension parameters of 0.4° to

¹ The location of the remnant is close to where the anchor (Latin: ancora) of Argo Navis would be in the constellation of Carina. Details can be found in Appendix A.

² github.com/fermi-lat/Fermitools-conda

³ slac.stanford.edu/exp/glast/groups/canda/lat_Performance.htm

⁴ TS is defined as twice the difference between log-likelihoods of source plus background (\mathcal{L}_1) and only background as a null hypothesis (\mathcal{L}_0): $TS = 2 \ln(\mathcal{L}_1/\mathcal{L}_0)$.

Table 1. List of the different models and their relative log-likelihood values compared to the base model, with $\mathcal{L}_0 = 435708.381$, and $\Delta \ln(\mathcal{L}) = \ln(\mathcal{L}_i) - \ln(\mathcal{L}_0)$, and the difference in model parameters compared to the base model ($\Delta k = k_i - k_0$).

Model N°	J1028 incl.	Spatial model	Spectral model	$\Delta \ln(\mathcal{L})$	Δk	ΔAIC
0	Y	–	–	0	0	0
1	N	–	–	–24.87	–5	39.74
2	Y	RadialDisk	PowerLaw	16.50	5	–22.99
3	N	RadialDisk	PowerLaw	9.54	0	–21.08
4	N	RadialDisk	LogParabola	9.80	1	–19.59
5	N	Radio template	PowerLaw	7.76	–1	–19.51

Notes. The two best-fit models presented in this work are marked in bold font.

1.5° in 21 logarithmic bins by performing a likelihood profile scan that maximises the model likelihood. The resulting best-fit extension was then added to the model, replacing the default value, and the whole region was refit again. The initial position from the radio detection was left unchanged to see spatial overlap with the radio source and determine the high-energy flux coming from that source region at this position, only varying the radius. We checked the source extension for a radial disk model and radial, symmetric two-dimensional (2D) Gaussian, and we fitted a smoothed radio template, using a power-law (PL) and a log-parabola (LP, Eq. (1)) spectral model.

The power-law spectral model used in *Fermipy* is of the form

$$\frac{dN}{dE} = N_0 \left(\frac{E}{E_0} \right)^{-\Gamma}, \quad (2)$$

with N_0 the normalisation or prefactor, Γ the spectral index, and E_0 the scaling energy. During the fitting the spectral parameters of the sources within 3° were left to vary.

We did not optimise the source position as the aim of this study was to test for a γ -ray source at the radio position. However, the radial size of the model was left to vary as the emission may be larger or smaller than the radio extension.

While performing the analysis it became clear that the *RadialGaussian* model was systematically overestimating the extension of the source by associating events previously modelled by the background or other sources with it, and subsequently reaching very high extensions ($\sim 1.5^\circ$). These extension results additionally varied strongly with different energy cuts. Even though the overall likelihood of the models seemed favourable, the authors agreed that the *RadialGaussian* model was not well behaved and was unsuitable for the purposes of the study. Thus, the analysis efforts were focused on the *RadialDisk* model, and the *RadialGaussian* results are not shown in this work.

3. Results

3.1. Comparing models

In this study, we tested different spatial models as well as two different spectral models for the best-fit model. A list of different iterations of the spatial models is shown in Table 1. The models were numbered starting with the base model (model 0) up to model 5. The second column indicates whether the model for J1028 was included in the fitting (Y) or not (N). The relative log-likelihoods $\ln(\mathcal{L}_i)$ compared to the base model $\ln(\mathcal{L}_0)$ are given, as well as the relative number of free fitting parameters k_i . Positive relative log-likelihood values indicate higher likelihood, and thus a better qualitative fit to the underlying data.

Lower values indicate a worse fit. Additionally, we show the value of the Akaike information criterion (AIC; Akaike 1974), a qualitative measure that indicates which of a number of different models is preferred over the others, taking into account the difference in free parameters. The $\text{AIC} = 2k - 2\ln(\mathcal{L})$ is presented in Table 1 as the difference between AIC values of different models, ΔAIC . Designated models are again compared to the base model ($\Delta \text{AIC} = \text{AIC}_i - \text{AIC}_0$).

Table 1 first shows the base model, the unchanged 4FGL-DR3 catalogue results (model 0) and then the identical model except that J1028 was removed from the modelling (model 1), as indicated by the second column, ‘J1028 incl.’. To model the excess, for models 2, 3, and 4, a *RadialDisk* spatial model was applied, including or excluding J1028 in the modelling⁵. Finally, we also show the performance of the model derived from the radio template (model 5).

3.2. Best-fit models and spatial results

The ΔAIC value for model 2 is the lowest, indicating that it is preferred over the other models (highlighted in bold font in Table 1). As this model includes the modelling of J1028, which lies within 0.7° of the centre of the SNR, it is quite possible that this excess is part of Ancora, and that a combination of the employed disk model together with the model for J1028 are the best description of the SNR.

We note that model 3 also obtained values close to the best model (also highlighted in bold in Table 1), although some unmodelled excess can be seen in the northern part of the shell. It is thus not entirely clear whether J1028 is actually associated with Ancora or is an unrelated source overlapping with the SNR. A spectral analysis (see below) shows that Ancora and J1028 have different spectral shapes, although given the limited photon counts this difference may not be significant.

The results of model 2 and model 3 (the *RadialDisk* spatial model, including and excluding the J1028 model from the source list, and a *PowerLaw* spectral model) are shown in Fig. 1. The figure shows the resulting significance maps within a field of view (FoV) of approximately $4.0^\circ \times 4.5^\circ$ for an energy range of 400 MeV–1 TeV, with overlays (2, 3, and 4 σ) of the resulting peaks above 1 GeV. In addition, the smoothed radio contours (Filipović et al. 2023) and the best-fit 0.92° radius for the models are also overlaid for easier orientation.

⁵ When adding the extended source, as in fit models 2–4, the catalogue sources as well as various background model normalisations can change as the overall region is optimised for maximising the log-likelihood value. Therefore, model 0 may differ from model 2 when removing the extended source after fitting, and the same applies for model 1 and models 3–4.

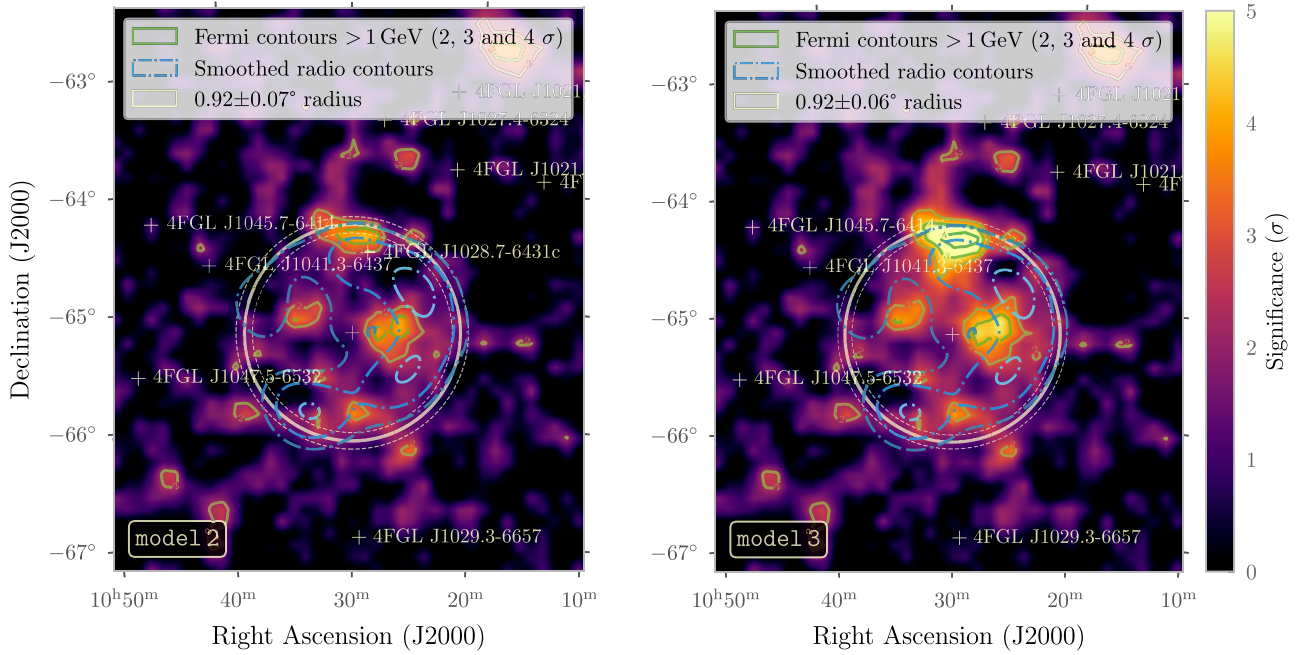


Fig. 1. Significance maps of the G288.8–6.3 region, as seen with *Fermi*-LAT, after fitting with a RadialDisk spatial model and a PowerLaw spectral model with (left, model 2) and without (right, model 3) modelling J1028 in the energy range of 400 MeV–1 TeV. The circles with radius 0.92° show the disk radius obtained from the respective fits. The plots show the significance map after subtracting all the fitted sources, except for the SNR. The maps are overlaid with Fermi contours for significance values above 1 GeV, and the smoothed radio contours from the ASKAP instrument at 954 MHz.

The significance maps both show an extended peak in γ -rays that coincides with the radio contours. Overall, the morphology is not identical: the high-energy emission is slightly more extended than the radio, and the clear shell morphology of the radio map is not seen in γ -rays. Flux contours for photons with energy above 1 GeV show much better correspondence with radio emission, tracing the western and northern parts of the shell in radio. To check the reliability of the extension fitting, an analysis for energies above 800 MeV was performed, which resulted in an extension of 0.91° , consistent with extensions found at lower energies.

3.3. Spectral results

The spectral energy distribution (SED) of the G288.8–6.3 region described with the RadialDisk model without modelling J1028 (model 3) extends up to 5 GeV and fits a PowerLaw spectral model with an energy flux of $(4.80 \pm 0.91) \times 10^{-6} \text{ MeV cm}^{-2} \text{ s}^{-1}$ (photon flux of $(3.14 \pm 0.41) \times 10^{-9} \text{ ph cm}^{-2} \text{ s}^{-1}$), and spectral index of $\Gamma = 2.32 \pm 0.11$, accounting only for statistical errors. The total significance of the source was estimated to be $\text{TS} = 77$, or an equivalent of $\sim 8.8\sigma$. The model improves the fit compared to the original catalogue with an increase of 9.54 in the log-likelihood value while maintaining the overall number of free parameters.

When examining the results for model 2 (including modelling for J1028) we find that the TS of the extended disk decreases to 45 (significance of 6.7σ), with most of this reduction corresponding to the addition of flux to J1028. For this model we find that the disk model also extends up to 5 GeV, and fits a PowerLaw spectral model with an energy flux of $(3.08 \pm 0.83) \times 10^{-6} \text{ MeV cm}^{-2} \text{ s}^{-1}$ (photon flux of $(2.29 \pm 0.45) \times 10^{-9} \text{ ph cm}^{-2} \text{ s}^{-1}$), and spectral index of $\Gamma = 2.21 \pm 0.12$. For J1028 we find an energy flux of

$(7.49 \pm 2.16) \times 10^{-7} \text{ MeV cm}^{-2} \text{ s}^{-1}$ (photon flux of $(9.68 \pm 3.08) \times 10^{-10} \text{ ph cm}^{-2} \text{ s}^{-1}$) with a total TS of 19.08 (significance of 4.4σ). Combining the model found for the SNR with the model for J1028, the total energy flux coming from this region is thus $\sim 5.04 \times 10^{-6} \text{ MeV cm}^{-2} \text{ s}^{-1}$ with a TS of 63.82 (8.0σ). This improves the overall likelihood by 16.50, and is the best-fit model of the region (model 2), slightly though possibly not significantly preferred over model 3. All values and a direct comparison between models 2, 3, and 5 can be found in Table 2.

Furthermore, the residual map for models 0 and 1 are shown in Fig. 2 (top left and top right, respectively), showing the relatively high level of extended residual flux that cannot be assigned to any of the sources in the 4FGL-DR3 catalogue. Figure 2 shows the residual maps for models 2 and 3 (bottom left and bottom right, respectively), where the extended emission from the Ancora SNR allows a much better fit to the data with lower residuals. We note that Fig. 2 (bottom left and bottom right, respectively) is the same model as Fig. 1 (left and right, respectively), but with the extended emission from Ancora removed. The SEDs for models 2 and 3 can be found in Fig. 3.

3.4. Multiwavelength modelling

The detection of Ancora SNR at radio wavelengths prompted the analysis of the G288.8–6.3 region. The radio spectral points are thus taken from Filipović et al. (2023). At X-ray energies Filipović et al. (2023) notes a non-conclusive result by eROSITA, as emission is detected uniformly from the whole region. We treat this result as a non-detection. None of our models predict any detectable non-thermal synchrotron radiation in the energy band that is observed by eROSITA (Merloni et al. 2012). The *Fermi*-LAT spectral points are taken from the

Table 2. Best-fit parameters of the RadialDisk model with and without modelling J1028 for Ancora SNR, as well as the results for the spatial template derived from the radio signal from the object.

Parameter	Unit	Value		
Position				
RA/Dec	deg/deg	157.488/−65.214		
GLON/GLAT	deg/deg	288.8/−6.3		
Model No.		2	3	5
J1028 incl.		Y	N	N
Spatial model		RadialDisk	RadialDisk	SpatialTemplate
Spectral model		PowerLaw	PowerLaw	PowerLaw
TS	–	44.74	77.14	70.98
N ^o of predicted photons	–	978	1331	1174
Photon flux	ph cm ^{−2} s ^{−1}	$(2.29 \pm 0.45) \times 10^{-9}$	$(3.14 \pm 0.41) \times 10^{-9}$	$(2.74 \pm 0.37) \times 10^{-9}$
Energy flux	MeV cm ^{−2} s ^{−1}	$(4.29 \pm 1.03) \times 10^{-6}$	$(4.80 \pm 0.91) \times 10^{-6}$	$(3.62 \pm 0.68) \times 10^{-6}$
> 1 GeV (to 316 GeV)	MeV cm ^{−2} s ^{−1}	$(3.08 \pm 0.83) \times 10^{-6}$	$(3.29 \pm 0.78) \times 10^{-6}$	$(2.13 \pm 0.66) \times 10^{-6}$
Spectral parameters				
N ₀	MeV ^{−1} cm ^{−2} s ^{−1}	$(9.17 \pm 1.81) \times 10^{-13}$	$(1.23 \pm 0.16) \times 10^{-12}$	$(1.15 \pm 0.15) \times 10^{-2}$
Γ	–	2.21 ± 0.12	2.32 ± 0.11	2.41 ± 0.13
E ₀	MeV	1000 ^(*)	1000 ^(*)	1000 ^(*)
Spatial parameters				
Extension	deg	0.92 ± 0.07	0.92 ± 0.06	–
TS _{ext} ^(†)	–	33.92	52.56	–

Notes. ^(*)Parameter fixed. ^(†)Test statistic for the extension hypothesis against the null hypothesis of a point-like source.

Table 3. *Naima* fit parameters.

Model	$W_{e/p}$ (erg) >1 GeV	s –	E_{cut} (GeV)	B_0 (μG)
2, leptonic	$1.6^{+0.6}_{-0.4} \times 10^{48}$	$2.0^{+0.1}_{-0.1}$	700^{+380}_{-260}	$6.4^{+1.9}_{-1.4}$
2, hadronic	$2.5^{+0.6}_{-0.5} \times 10^{50}$	$2.4^{+0.3}_{-0.2}$	–	–
3, leptonic	$2.9^{+1.5}_{-0.9} \times 10^{48}$	$1.93^{+0.07}_{-0.08}$	400^{+200}_{-130}	$4.4^{+1.5}_{-1.3}$
3, hadronic	$3.5^{+0.9}_{-0.7} \times 10^{50}$	$2.50^{+0.23}_{-0.14}$	–	–

Notes. We used an exponentially cutoff power-law model for the underlying electron and proton distributions to fit the data points of model 2 and model 3.

best-fit model using the PowerLaw spectral model with and without modelling J1028 (models 2 and 3).

We investigated a leptonic inverse Compton (IC) and a hadronic pion decay (PD) scenario for the γ -ray emission, and performed *Naima* modelling (Zabalza 2015) assuming a power-law distribution of electrons with an exponential cutoff or a power-law distribution for protons. In the latter case, a cutoff cannot reliably be fit due to the lower number of significant data points.

The fit parameters for the underlying particle populations are presented in Table 3, and the resulting emission spectra in Fig. 4. We note that the hadronic models do not constrain the electron populations and that hence the values of the magnetic field strength B_0 and total energy in electrons W_e for the corresponding leptonic models represent lower and upper limits, respectively. We used $n = 0.15 \text{ cm}^{-3}$ as the density of the target material in the hadronic model, taken from within the

range of $0.11\text{--}0.24 \text{ cm}^{-3}$, as estimated by Filipović et al. (2023) using Wolfire et al. (2003).

The fit parameters for source model 2 and model 3 are very similar and overlap within their respective uncertainties, so we discuss them together. We find that the energy in electrons is approximately 0.25% of the initial assumed explosion energy of 10^{51} erg; these are typical values expected from a source like the one presented. The spectral index $s \approx 2$, which is mainly determined by signal in the radio bands, matches the canonical expectation for diffusive shock acceleration (DSA).

The cutoff is only weakly constrained. Because of the limited photon counts, we are not able to distinguish between a spectral break and a cutoff. Before we can draw any definite conclusions, observations at very high γ -ray energies (VHE) are needed. The magnetic field is found to be lower than estimates by Filipović et al. (2023). However, it is roughly comparable with the shock-compressed weak interstellar medium (ISM) field of $B_0 \leq 3 \mu\text{G}$ as an off-plane source.

Due to the low gas density inferred from analysis of the radio observations (Filipović et al. 2023), pion decay models require a rather large energy budget in CRs of 30% of the explosion energy. Taken at face value, this makes a leptonic scenario favourable based on the required energy in electrons and protons. Additionally, it was found in earlier studies that leptonic remnants in low-density environments tend to reach a higher peak luminosity in γ -rays (Brose et al. 2021). Only the cosmic microwave background (CMB) was considered as the contributing photon field as the object is an off-plane remnant. However, the energy in protons scales linearly with the ambient density, so that a higher ambient density could resolve this tension for the hadronic model. MOPRA observations show an increasing density towards Ancora (Braiding et al. 2018), but the remnant itself is not covered in the observations. In contrast, a density of 0.4 cm^{-3} is close to the environment of *Tycho*, which is also

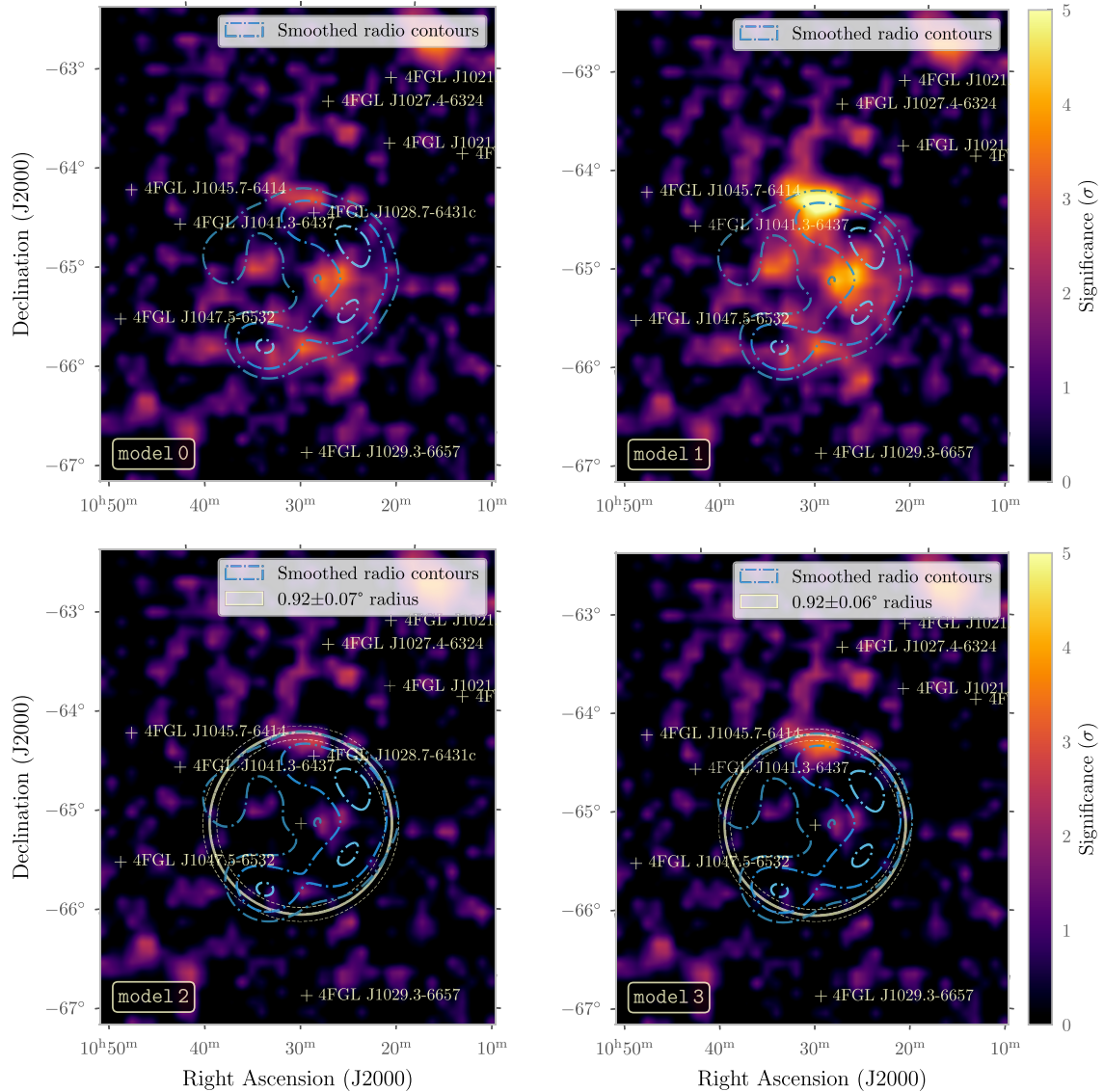


Fig. 2. Residual maps of the G288.8–6.3 region around Ancora SNR, as seen with *Fermi*-LAT. *Top row:* residual maps of model 0 (top left, obtained directly from the 4FGL-DR3 catalogue) and model 1 (top right). *Bottom row:* residual maps for model 2 (bottom left) and model 3 (bottom right, position of J1028 marked for reference), after adding a RadialDisk spatial model and a PowerLaw spectral model and refitting. All fits were in the energy range of 400 MeV–1 TeV. The blue contours show smoothed radio emission. Models 0 and 1 show γ -ray excess overlapping with this region. The circles with radius 0.92° in the bottom panels show the disk radius obtained from the fits of models 2 and 3. The top and bottom panels represent different fits as the region is refit after adding the extended SNR model. The bottom panels represent the exact fit shown in Fig. 1, except for the removal of the extended model.

inferred to be farther away, where clear signatures of thermal X-ray emission are detected. The eROSITA image of Ancora in Filipović et al. (2023) shows no sign of enhanced emission from the remnant. Additional investigations of the X-ray emission and gas density around Ancora are clearly needed to resolve this issue.

4. Discussion

4.1. Distinguishing between different models describing the γ -ray excess

Although model 2 is statistically slightly favoured over model 3, it seems that overall they are fairly similar in terms of ΔAIC , and a significant preference for one over the other is not given. There is no conclusive evidence to assume that J1028 is

actually a separate source. When modelling J1028 together with an overlapping disk, its significance decreases from the catalogue value of 5.6σ to 4.4σ , below the threshold of what is commonly assumed to be significant in the field. Additionally, modelling an extended disk together with J1028 provides a substantial number of additional degrees of freedom to the overall model. The combined flux from the region is significantly improved when only modelling one extended source. The authors of this work therefore tend to favour the simpler scenario with only one extended model (model 3).

4.2. Comparison with other high-latitude SNRs

With Ancora we add another object to the list of known SNRs emitting γ -rays at GeV energies located at high Galactic latitudes. It joins other known sources off the Galactic

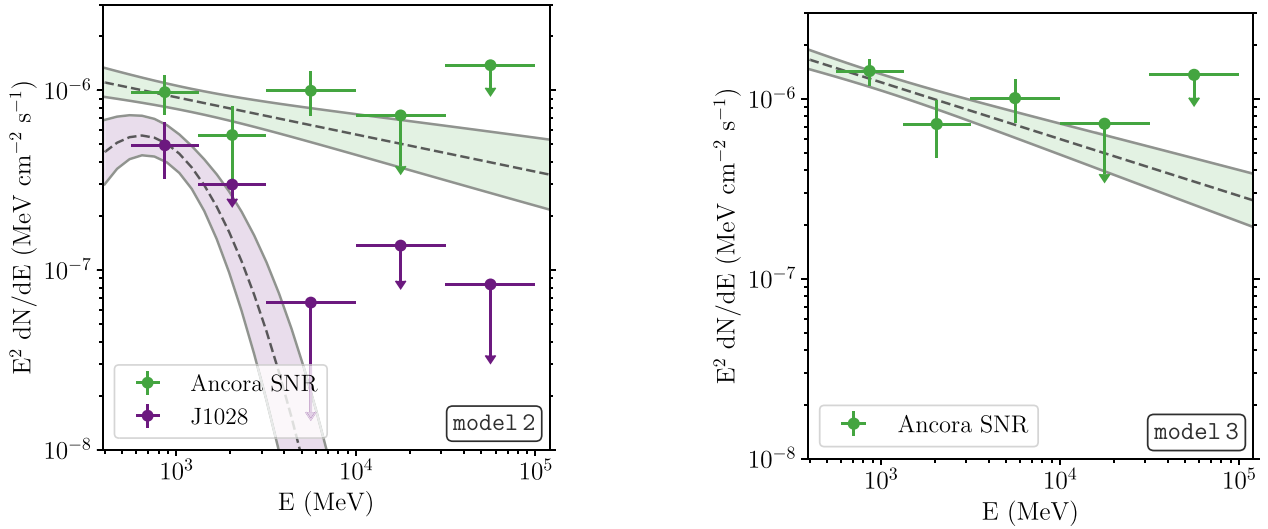


Fig. 3. Spectral energy distribution of the G288.8–6.3 region using a RadialDisk spatial model and a PowerLaw with (left, model 2) and without (right, model 3) modelling J1028. Additionally, the spectral models as well as their 1σ uncertainty bands are shown in the respective colours of the spectral points.

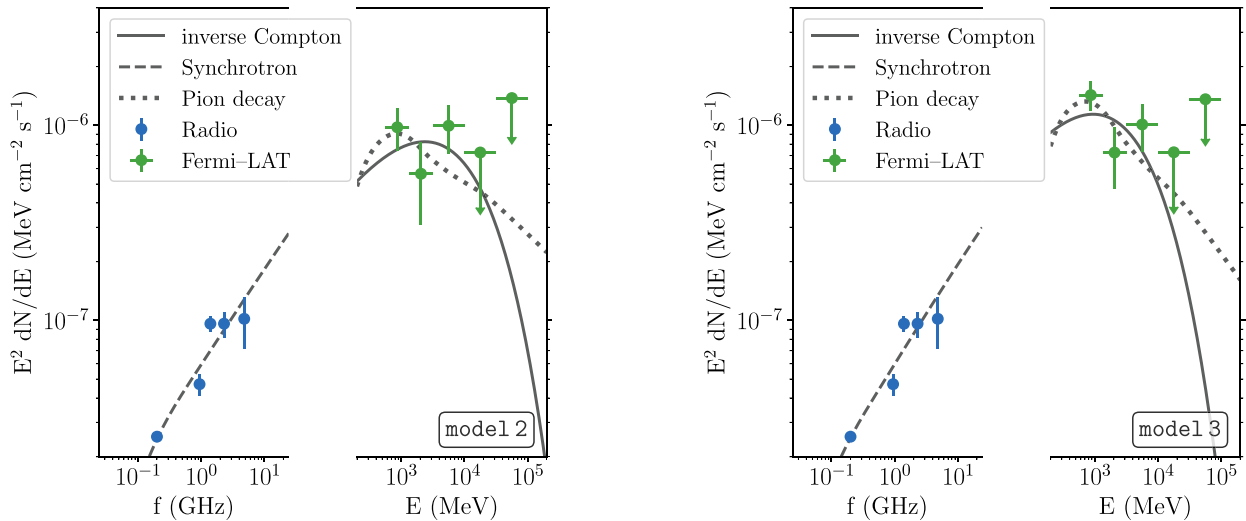


Fig. 4. Multiwavelength SED from G288.8–6.3. The blue points are radio-flux measurements from Filipović et al. (2023), and the green points are the *Fermi*-LAT data points representing model 2 (left) and model 3 (right). The curves represent the best-fit *Naima* models with the particle population parameters indicated in Table 3. The solid curves represent the synchrotron emission, the dashed curves the inverse-Compton emission, and the dotted curves the Pion-decay emission.

plane, such as SN 1006 (Condon et al. 2017), G296.5+10.0 (Araya 2013; Ackermann et al. 2018), and G166.0+4.3 (Araya 2013). We collected the high-energy data from different publications in Table 4, where we took the spectral fits quoted and re-calculated the energy flux for the energy range 1 GeV–1 TeV, consistent with Ackermann et al. (2018). The source FHES J1741.6–391 was previously associated with a SNR (Ackermann et al. 2018); however, it is currently not confirmed as such⁶, and has thus not been included in Table 4.

For Ancora SNR we obtained a photon spectral index of $\Gamma \approx 2.3$. This value lies between the results previously found for other high-latitude SNRs, such as Calvera SNR

(Arias et al. 2022; Araya 2023) with $\Gamma = 1.66$ at one extreme and G166+4.3 with $\Gamma = 2.7$ (Araya 2013) at the other. The location of these SNRs far from the Galactic plane, and thus in potentially lower-density environments could make leptonic emission scenarios more likely for them. The observed range of photon spectral indices is not constraining in this regard as hard spectral indexes of $\Gamma \approx 1.5$ are expected for a canonical DSA-accelerated electron spectrum of $s = 2$; intermediate indexes around $\Gamma \approx 2$ for SNRs with substantial cooling and a potential mix of different electron populations (Sushch et al. 2022); and soft spectral indices of $\Gamma \approx 2.7$ for cases where particles escape a fading accelerator (Brose et al. 2021).

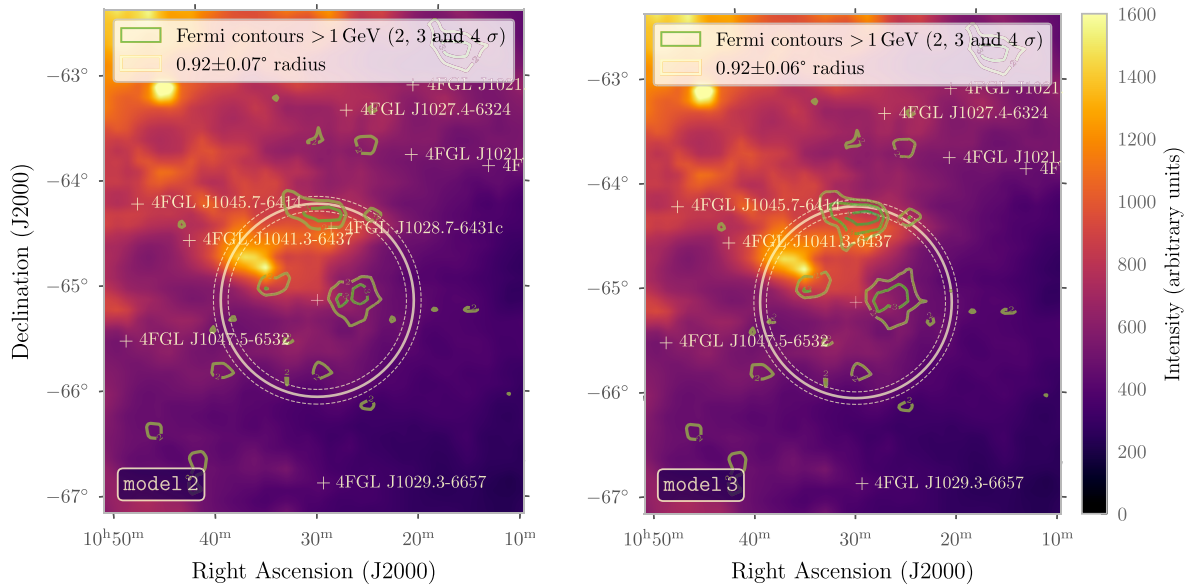
When comparing the energy fluxes, the lowest flux of $\approx 2.87 \times 10^{-6} \text{ MeV cm}^{-2} \text{ s}^{-1}$ was found for G166.0+4.3 and the highest flux of $\approx 5.20 \times 10^{-5} \text{ MeV cm}^{-2} \text{ s}^{-1}$ was found for G150+4.5, which also has the largest angular size. The energy

⁶ It has been found to have an extension radius of $15'$ at radio wavelengths (Green 2019), compared to the extension of 1.35° in γ -rays (Ackermann et al. 2018). Due to the large angular size difference it is not clear if the two are physically related.

Table 4. Comparison of Ancora SNR to fluxes and photon spectral indices of other known high-latitude SNRs detected at high energies, sorted by their total energy flux.

Source name	Extension (deg)	Energy flux (MeV cm ⁻² s ⁻¹) 1 GeV–1 TeV	Photon spectral index –	Reference
Ancora SNR/G288.8–6.3	0.92	$(3.29 \pm 0.78) \times 10^{-6(\perp)}$	$2.31 \pm 0.11^{(\perp)}$	This work
G150+4.5	1.5	$5.20 \times 10^{-5(*)}$	$1.62 \pm 0.04_{\text{stat}} \pm 0.22_{\text{sys}}^{(\dagger)}$	Devin et al. (2020)
G17.8+16.7/ FHES J1723.5–0501	0.73	$(1.38 \pm 0.26) \times 10^{-5(\nabla)}$	$1.83 \pm 0.02_{\text{stat}} \pm 0.05_{\text{sys}}$ $1.97 \pm 0.08_{\text{stat}} \pm 0.06_{\text{sys}}$	Araya et al. (2022) Ackermann et al. (2018)
G296.5+10.0/FHES J1208.7–5229	0.7	$8.17 \times 10^{-6(**)}$ $(1.13 \pm 0.24) \times 10^{-5(\nabla)}$	1.85 ± 0.13 $1.81 \pm 0.09_{\text{stat}} \pm 0.05_{\text{sys}}$	Araya (2013) Ackermann et al. (2018)
SN 1006/G327.6+14.6	0.1	$(3.63 \pm 1.62) \times 10^{-6(\dagger\dagger)}$	1.57 ± 0.11	Condon et al. (2017)
Calvera SNR/G118.4+37.0	0.53	$3.06 \times 10^{-6(\nabla\nabla)}$	$1.66 \pm 0.10_{\text{stat}} \pm 0.03_{\text{sys}}$	Araya (2023)
G166+4.3	~0.3	$2.87 \times 10^{-6(**)}$	2.7 ± 0.1	

Notes. The list includes data from the SNR catalogue provided by Ferrand & Safi-Harb (2012). ^(\circ)snrcat.physics.umanitoba.ca; ^(\perp) values taken from model 3, energy range 1 GeV–316 GeV; ^(*)calculated using data from Table 2 in Devin et al. (2020), and using results for the radial Gaussian model and log-parabola spectral model; ^(\dagger)log-parabola model, α given in Table, $\beta = 0.07 \pm 0.02_{\text{stat}} \pm 0.02_{\text{sys}}$; ^(\nabla) from FITS data provided with Ackermann et al. (2018); ^(**)calculated using data from Table 2 in Araya (2013); ^(\dagger\dagger)range is 1 GeV–2 TeV; ^(\nabla\nabla)calculated using data from Araya (2023).

**Fig. 5.** Thermal, unpolarised dust emission map produced by the *Planck* mission (Planck Collaboration X 2016), overlaid with *Fermi*-LAT contours above 1 GeV of Ancora SNR (model 2 (left) and model 3 (right)) and their respective spatial extension.

flux of the Ancora SNR puts it on the lower end of the range (see Table 4). Obtaining the physical luminosity and size of these remnants requires a good estimate of their distance which in most cases is not available, but at least from the spectral index it appears that the Ancora SNR provides an ‘in-between’ example connecting the hard- and soft-spectrum sources. This may be an indication that it has an intermediate age among the detected SNRs.

4.3. Possibility of interaction with interstellar clouds

The extended *Fermi*-LAT source J1028 has the letter ‘c’ appended to its catalogue designation, indicating possible association with molecular clouds along the line of sight. This possibility was investigated using the thermal unpolarised

dust emission maps produced by the *Planck*⁷ mission (Planck Collaboration X 2016). The map was downloaded from the NASA/IPAC Infrared Science Archive⁸ and the contours of *Fermi*-LAT emission were overlaid (see Fig. 5). A general gradient can be seen, with dust emission increasing strongly towards the Galactic plane (to the north-east).

There is significant dust emission in the region of G288.8–6.3, partially overlapping with the location of J1028, but the lack of clear correlation with the dust disfavors in principle

⁷ Based on observations obtained with *Planck* (esa.int/Planck), an ESA science mission with instruments and contributions directly funded by ESA Member States, NASA, and Canada.

⁸ irsa.ipac.caltech.edu/data/Planck/release_2/all-sky-maps/foregrounds.html

a sizeable hadronic contribution. However, more observations with precise imaging could still reveal denser clumps of gas (Fukui et al. 2012), provided that the whole region seems to have a higher dust level than expected at such a high latitude. Based on this map (Fig. 5) we expect that leptonic emission is a more likely explanation for the GeV emission detected from G288.8–6.3. Near the region of J1028, it could be that the SNR is interacting with dense gas, and hence that some of the emission from this part of the remnant is hadronic, but this can be neither confirmed nor disproved with the data available. Further observations of the gas and dust distribution around G288.8–6.3 together with a search for thermal X-ray emission are needed to clearly disentangle any hadronic contribution.

4.4. Interpretation of the high-energy morphology

The extension of the γ -ray emission at around 0.9° seems to be slightly larger than that detected at radio wavelengths at about 0.8° . This is also observed in the Calvera SNR (Arias et al. 2022; Araya 2023) and G17.8+16.7 (Ackermann et al. 2018; Araya et al. 2022), and can be explained by the escape of CRs from an evolved SNR (Brose et al. 2021). The SNR shock compresses the ambient field, giving rise to radio emission through the synchrotron process in the downstream of the shock, whereas escaping electrons can interact with the uniformly distributed ambient photons of the CMB through IC interaction to produce γ -rays at much larger distances from the SNR shell. Thus, the radio and γ -ray morphology can differ quite significantly, as the synchrotron emission tracks only a sub-population of the electrons accelerated in the Ancora SNR. In that sense, the magnetic field derived by our modelling (see Table 3) represents a lower limit to the magnetic field strength in the Ancora SNR. A significantly larger extension of G288.8–6.3 in VHE γ -rays can be expected in this scenario. However, based on the observational uncertainties of the measured extension, no firm claim can be made at the moment that the γ -ray emission is larger than the radio extension.

Additionally, further data at very high energies (VHE, >100 GeV) for these high-latitude SNRs would strongly constrain the emission processes through spectral modelling (see Fig. 4) and close the gap in observational data between the young historical remnants and old SNRs interacting with molecular clouds (Zeng et al. 2019). The typically large extension of these high-latitude SNRs simplifies morphological comparisons between radio, high-energy, and VHE emission, and provides valuable information to understand CR escape to the ISM. An extrapolation of the GeV-flux data to TeV energies suggests that the Ancora and other high-latitude SNRs may be detectable with imaging atmospheric Cherenkov telescopes (IACTs) and potentially also water Cherenkov detectors.

To date, SNRs with confirmed hadronic emission signatures have only been observed in the Galactic plane and interacting with molecular clouds in high-density regions (Ackermann et al. 2013; Zeng et al. 2019). It is expected, however, that signatures of CR escape (spectral breaks in the 1–100 GeV range and soft spectra at higher energies) are also present without such special circumstances, and depend on the age of the remnant (Brose et al. 2021). SNRs at high Galactic latitudes such as the Ancora SNR can help to build an unbiased picture of the evolution of particle acceleration and escape in SNRs.

5. Conclusions

Prompted by the recent discovery of a SNR at high Galactic latitude with ASKAP, we reanalysed the G288.8–6.3 region with

the *Fermi*-LAT instrument and detected a highly extended high-energy γ -ray source coinciding with the radio position. Different spatial and spectral models were tested in the process. It was found that two models are quite closely favoured, both fitting the excess using a radial disk spatial model and a power-law spectral model. The two scenarios (models 2 and 3) only differ in whether or not they include the modelling for J1028, an unidentified *Fermi* catalogue source that lies within 0.7° of the SNR centre. Energy flux estimates for model 2 return values of $(4.29 \pm 1.03) \times 10^{-6} \text{ MeV cm}^{-2} \text{ s}^{-1}$ (photon flux of $(2.29 \pm 0.45) \times 10^{-8} \text{ ph cm}^{-2} \text{ s}^{-1}$) and a spectral index $\Gamma = 2.21 \pm 0.12$, and a significance of 6.7σ , while J1028, modelled by a log-parabola spatial model is left with a significance of 4.4σ , an energy flux of $(7.49 \pm 2.16) \times 10^{-7} \text{ MeV cm}^{-2} \text{ s}^{-1}$ (photon flux of $(9.68 \pm 3.08) \times 10^{-10} \text{ ph cm}^{-2} \text{ s}^{-1}$), resulting in a total energy flux of $\sim 5.04 \times 10^{-6} \text{ MeV cm}^{-2} \text{ s}^{-1}$ with a total significance of 8.0σ , if we assume that the two sources combined can both be attested to emission from the SNR. Considering model 3, we measured an energy flux of $(4.80 \pm 0.91) \times 10^{-6} \text{ MeV cm}^{-2} \text{ s}^{-1}$ (photon flux of $(3.14 \pm 0.41) \times 10^{-8} \text{ ph cm}^{-2} \text{ s}^{-1}$) and a spectral index $\Gamma = 2.32 \pm 0.11$. In both cases, the spectrum extends to around 5 GeV. Morphological hotspots above 1 GeV are well correlated with the bright western part of the radio shell. The best-fit extension was found to be $\sim 0.92^\circ$, slightly larger than the radio shell at around 0.8° , as was expected from theory. Given the estimated gas density in the region, the estimated distance and age of the SNR, and the total energy arguments, the emission is more likely to be of leptonic origin, but a hadronic scenario cannot be ruled out based on the incomplete picture of the gas-distribution around Ancora.

The observations were put in a multi-wavelength context by using *Naima* modelling. We found that either a electron distribution with an exponential cutoff at $E_{\text{max}} = (700^{+380}_{-260}) \text{ GeV}$ ($E_{\text{max}} = (400^{+200}_{-130}) \text{ GeV}$), a spectral index of $s = 2.0 \pm 0.1$ ($s = 1.93 \pm 0.07$), and a total energy of $W_e = 1.6^{+0.6}_{-0.4} \times 10^{48} \text{ erg}$ ($W_e = 2.9^{+1.5}_{-0.9} \times 10^{48} \text{ erg}$) in electrons above 1 GeV describes the emission well when the magnetic-field strength is $B_0 = 6.4^{+1.9}_{-1.4} \mu\text{G}$ ($B_0 = 4.4^{+1.5}_{-1.3} \mu\text{G}$) for our models including (excluding) J1028. A hadronic scenario with $s = 2.4^{+0.3}_{-0.2}$ ($s = 2.50^{+0.23}_{-0.14}$) and a total energy of $W_p = 2.6^{+1.1}_{-0.6} \times 10^{50} \text{ erg}$ ($W_p = 3.5^{+0.9}_{-0.7} \times 10^{50} \text{ erg}$) in protons yields a similarly good fit. The cutoff energy, however, cannot be constrained in that case.

Ancora is only the seventh confirmed SNR detected at high Galactic latitude with *Fermi*-LAT. This new population of remnants has the potential to constrain the physics of particle diffusion and escape from SNRs into the Galaxy. Due to their narrow field of view of a few degrees, IACTs usually only observe off the Galactic plane if clear indications of emission from these regions are given. Extrapolating the energy flux and considering the brightness of the Ancora SNR, this object may be observable with current IACTs such as H.E.S.S., and should be easily detectable with next-generation IACTs such as the Cherenkov Telescope Array (CTA), and possibly future water Cherenkov detectors, such as the Southern Wide-field Gamma-ray Observatory (SWG0).

Acknowledgements. C.B.S. acknowledges support from a Royal Society-Science Foundation Ireland Research Fellows Enhancement Award 2021 (22/RS-EA/3810). This work was supported by an Irish Research Council (IRC) Starting Laureate Award (IRCLA/2017/83). R.B. acknowledges funding from the Irish Research Council under the Government of Ireland Postdoctoral Fellowship program. J.M. acknowledges support from a Royal Society – Science Foundation Ireland University Research Fellowship (20/RS-URF-R/3712) M.D.F., G.R. and S.L. acknowledge Australian Research Council funding through grant

DP200100784. I.S. acknowledges support by the National Research Foundation of South Africa (Grant Number 132276). This work makes use of publicly available *Fermi*-LAT data provided online by the *Fermi* Science Support Center at fermi.gsfc.nasa.gov/ssc/, as well as publicly available data obtained with *Planck* (esa.int/Planck), an ESA science mission. This research made use of *Fermitools* (github.com/fermi-lat/Fermitools-conda), as well as the following Python packages: *Fermipy* (Atwood et al. 2013), *Astropy* (Astropy Collaboration 2022), *Numpy* (Harris et al. 2020), and *Matplotlib* (Hunter 2007). Access to the scripts used to produce this work will be made available upon contact with the first author. Special thanks to M. Lemoine-Goumard, J. Devin and Q. Remy for fruitful discussions. We also want to thank the anonymous reviewer for helpful comments improving the manuscript. C.B.S. would like to dedicate this work to Daniel R.W. Bale, who, through his creative and unconventional yet highly systematic approach to experiments and projects in various fields, paired with his profound curiosity, shaped the lives of many whose paths he crossed.

References

- Abdollahi, S., Acero, F., Ackermann, M., et al. 2020, *ApJS*, **247**, 33
- Abdollahi, S., Acero, F., Baldini, L., et al. 2022, *ApJS*, **260**, 53
- Abeyssekara, A. U., Archer, A., Benbow, W., et al. 2020, *ApJ*, **894**, 51
- Acero, F., Ackermann, M., Ajello, M., et al. 2016, *ApJS*, **224**, 8
- Ackermann, M., Ajello, M., Allafort, A., et al. 2013, *Science*, **339**, 807
- Ackermann, M., Ajello, M., Baldini, L., et al. 2018, *ApJS*, **237**, 32
- Aharonian, F., Akhperjanian, A. G., Bazer-Bachi, A. R., et al. 2007, *ApJ*, **661**, 236
- Akaike, H. 1974, *IEEE Trans. Automatic Control*, **19**, 716
- Aloisio, R., Berezhinsky, V., & Gazizov, A. 2012, *Astrop. Phys.*, **39**, 129
- Araya, M. 2013, *MNRAS*, **434**, 2202
- Araya, M. 2023, *MNRAS*, **518**, 4132
- Araya, M., Hurley-Walker, N., & Quirós-Araya, S. 2022, *MNRAS*, **510**, 2920
- Arias, M., Botteon, A., Bassa, C. G., et al. 2022, *A&A*, **667**, A71
- Astropy Collaboration (Price-Whelan, A. M., et al.) 2022, *ApJ*, **935**, 167
- Atwood, W., Albert, A., Baldini, L., et al. 2013, *Pass 8: Toward the Full Realization of the Fermi-LAT Scientific Potential*
- Baade, W., & Zwicky, F. 1934, *PNAS*, **20**, 259
- Braiding, C., Wong, G. F., Maxted, N. I., et al. 2018, *PASA*, **35**, e029
- Brose, R., Pohl, M., & Sushch, I. 2021, *A&A*, **654**, A139
- Condon, B., Lemoine-Goumard, M., Acero, F., & Katagiri, H. 2017, *ApJ*, **851**, 100
- Delporte, E. 1930, *Délimitation scientifique des constellations: (tables et cartes)*, Report/Commission 3 of the International Astronomical Union (Cambridge University Press)
- Devin, J., Lemoine-Goumard, M., Grondin, M. H., et al. 2020, *A&A*, **643**, A28
- Esposito, J. A., Hunter, S. D., Kanbach, G., & Sreekumar, P. 1996, *ApJ*, **461**, 820
- Ferrand, G., & Safi-Harb, S. 2012, *Adv. Space Res.*, **49**, 1313
- Filipović, M. D., Dai, S., Arbutina, B., et al. 2023, *AJ*, **166**, 149
- Filipović, M. D., & Tothill, N. F. H. 2021, *Multimessenger Astronomy in Practice* (IOP Publishing), 2514
- Fukui, Y., Sano, H., Sato, J., et al. 2012, *ApJ*, **746**, 82
- Globus, N., Allard, D., & Parizot, E. 2015, *Phys. Rev. D*, **92**, 021302
- Green, D. A. 2017, *VizieR Online Data Catalog: VII/278*
- Green, D. A. 2019, *A&A*, **40**, 36
- Harris, C. R., Millman, K. J., van der Walt, S. J., et al. 2020, *Nature*, **585**, 357
- Hess, V. F. 1912, *Phys. Zeitsch.*, **13**, 1084
- H.E.S.S. Collaboration (Abdalla, H., et al.) 2018, *A&A*, **612**, A3
- Hunter, J. D. 2007, *Comput. Sci. Eng.*, **9**, 90
- Lacaille, de, N.-L. 1755, *Mem. Acad. R. Sci.*, 194
- Merloni, A., Predehl, P., Becker, W., et al. 2012, arXiv e-prints [arXiv:1209.3114]
- Planck Collaboration X. 2016, *A&A*, **594**, A10
- Ptolemy, Toomer, G. J., & Gingerich, O. 1998, *Ptolemy's Almagest* (Princeton University Press)
- Ridpath, I. 2018, *Star Tales*, 1st edn. (The Lutterworth Press)
- Sturmer, S. J., & Dermer, C. D. 1995, *A&A*, **293**, L17
- Sushch, I., Brose, R., Pohl, M., Plotko, P., & Das, S. 2022, *ApJ*, **926**, 140
- Tanabashi, M., Hagiwara, K., Hikasa, K., et al. 2018, *Phys. Rev. D*, **98**, 030001
- Vink, J. 2012, *A&A Rev.*, **20**, 49
- Wolfire, M. G., McKee, C. F., Hollenbach, D., & Tielens, A. G. G. M. 2003, *ApJ*, **587**, 278
- Wood, M., Caputo, R., Charles, E., et al. 2017, in *International Cosmic Ray Conference, 35th International Cosmic Ray Conference (ICRC2017)*, 301, 824
- Zabalza, V. 2015, *Proceedings of International Cosmic Ray Conference 2015*, 922
- Zeng, H., Xin, Y., & Liu, S. 2019, *ApJ*, **874**, 50
- Zotti, G., & Wolf, A. 2023, *J. Skyscape Archaeol.*, **8**, 332

Appendix A: Naming of Ancora SNR

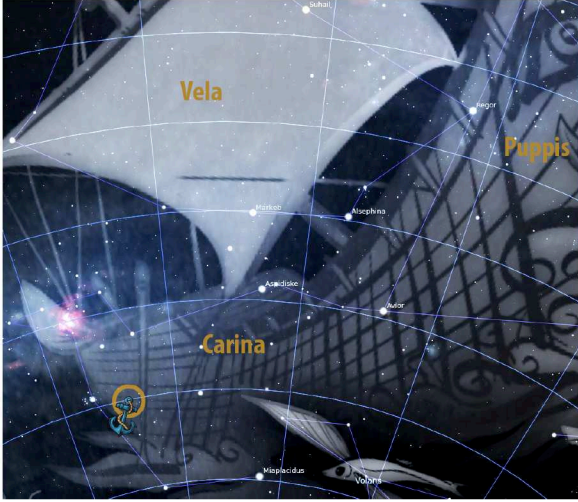


Fig. A.1: *Ancora* in the context of *Argo navis*, marked with a gold circle around the G288.8–6.3 position. Graphics: Stellarium (Zotti & Wolf 2023) and pngggg.

Historically, *Argo navis* (in English, the ship Argo) was one of the 48 constellations of Ptolemy (Ptolemy et al. 1998). The name Argo refers to the ship Argo in Greek mythology, in which Jason and his crew, the Argonauts, sailed to Colchis, a place on the shores of the Black Sea, to recover the Golden Fleece (Ridpath 2018). In 1930 at the meeting of the International Astronomical Union (IAU) where the decision on settling on the modern 88 constellations was made (Delparte & International Astronomical Union 1930), it was officially broken up into three distinct constellations, as had been suggested by Nicolas Louis de Lacaille in his 1755 catalogue (Lacaille 1755): *Puppis*, the poop deck or stern; *Vela*, the sail; and *Carina*, the keel. *Argo navis* was officially retired.

The supernova remnant discussed in this work at $\text{GLON/GLAT} = 288.8^\circ / -6.3^\circ$ is located in the constellation of *Carina*, towards the front of the keel, a position where the anchor of a ship would usually be found. To keep in line with Latin naming traditions, the Latin term for anchor, *ancora*, was henceforth used to distinguish the SNR from others. An artist's impression of the anchor in context can be found in Fig. A.1.